

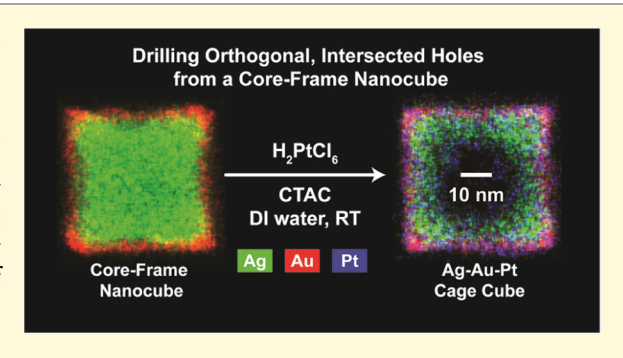
Fabrication of Nanoscale Cage Cubes by Drilling Orthogonal, Intersected Holes through All Six Side Faces of Ag Nanocubes

Jaewan Ahn and Dong Qin*®

School of Materials Science and Engineering, Georgia Institute of Technology, Atlanta, Georgia 30332, United States

Supporting Information

ABSTRACT: We report a general method based on the galvanic replacement for the fabrication of nanoscale, multimetallic, cage cubes by confining the drilling of Ag to the center of each side face of a Ag nanocube encased by Ag-Au alloy frames. In a typical process, we disperse Ag@Ag-Au core-frame nanocubes in an aqueous solution of cetyltrimethylammonium chloride, followed by the titration of an aqueous solution of the precursor under ambient conditions. We identify that the oxidation of Ag is preferentially instigated from the Ag-dominated regions located at the center of each side face of a nanocube for the creation of a cavity, while the resultant metal atoms are deposited on the edges and corners in an orthogonal manner. In the case of H₂PtCl₆ precursor, Ag atoms will



be carved away from the side faces in the form of Ag(I) ions for the generation of a much smaller number of Pt atoms. Because a thin layer of Ag-Au-Pt alloy tends to be formed on the surface, including the areas around but not inside the cavities, it is possible to achieve continuous removal of Ag toward the center of a core-frame nanocube for its ultimate transformation into a cage cube composed of a Ag-Au-Pt alloy and characterized by three orthogonal, intersected holes. The same strategy also works for other salt precursors, including Pt(II), Pd(II), and Au(III), but the size of the holes may vary depending on the stoichiometry involved in the galvanic replacement reaction.

1. INTRODUCTION

Noble-metal nanocrystals with well-controlled morphologies and compositions have enabled a range of applications in biomedicine, ¹⁻³ catalysis, ⁴⁻⁶ optical sensing, ^{7,8} and surfaceenhanced Raman scattering. 9-12 Among the synthetic methods, galvanic replacement relies on a simple redox reaction to transform solid mono- or bimetallic nanocrystals of various shapes into hollow and/or porous metallic nanostructures. For example, Ag nanocubes were reacted with a Au(I) or Au(III) precursor in an aqueous solution for the production of Ag-Au nanoboxes and nanocages with tunable optical properties. 13,14 Similar approaches have been successfully applied to the generation of hollow and/porous nanostructures made of Ag-Pt, ¹⁵ Ag-Pd, ¹⁶ and Pd-Pt, ¹⁷ and some of these nanostructures were further explored for catalytic applications. When combined with the Kirkendall effect, galvanic replacement has also been employed to convert Ag nanocubes into double-walled nanoboxes with different exterior and interior compositions. 18,19

In recent years, many groups have explored the spatial separation of the galvanic replacement reaction on a nanoscale surface for the fabrication of nanostructures with increasingly complex morphologies and compositions. To this end, Xia and co-workers observed that the oxidation of Ag could be initiated from the {111} facets or corner sites of truncated Ag nanocubes when they were reacted with a Au(III) precursor in the presence of poly(vinylpyrrolidone) (PVP). 13 They also

reported the fabrication of Pd-Pt concave nanocubes through the galvanic replacement reaction between Pd nanocubes and a Pt(IV) precursor.²⁰ It was shown that the Br⁻ ions in the reaction solution could selectively bind to and activate the {100} facets on Pd nanocubes, leading to the oxidation of Pd from the {100} facets or side faces for the deposition of Pt on the {111} facets or corners in an orthogonal manner. Liz-Marzan and co-workers reported a detailed analysis of the structural evolution of Ag nanocubes when they were reacted with HAuCl₄ in an organic solvent, together with the use of Cl ions. 21 Using electron tomography, they were able to capture the generation of a small pinhole on the side faces of nanocubes at the early stage of synthesis, confirming that the oxidation of Ag was also initiated from the side faces due to the selective binding of Cl⁻ ions to the {100} facets. ^{22,23} As the reaction progressed, they revealed that the oxidation of Ag atoms was continued from the center of each side face for the generation of gradually enlarged holes while the resultant Au atoms were deposited on the other regions of a nanocube, leading to the generation of octahedral nanocages made of Ag-Au alloys. Most recently, we investigated the site selectivity of the galvanic replacement reaction between Ag nanocubes and a Au(III) or Pd(II) precursor in the presence

Received: September 16, 2019 Revised: October 18, 2019 Published: October 20, 2019



of Cl⁻ ions, during which Ag oxidation occurred at the {100} facets of nanocubes for the deposition of Au or Pd atoms on the {110} and {111} facets and thus the formation of Ag–Au or Ag–Pd concave nanocubes.^{24,25}

In addition to these studies involving the use of monometallic nanocrystals as templates with surface inhomogeneity associated with faceting and/or capping, bimetallic systems with spatially controlled distributions of elements were also explored in recent years. ^{26,27} In one study, Skrabalak and co-workers used Ag-Pd dimers with a Janus structure as templates to react with various Au(III) precursors having different reduction potentials in the presence of PVP.²⁶ They demonstrated that the replacement of Ag was more rapid than that of Pd, leading to the creation of Ag vacancies as the Au atoms were deposited on the Ag surface. Because some of the Ag vacancies would diffuse into Pd to generate a Ag-Pd alloy, the subsequent oxidation of Ag by the Au(III) precursor would progress on both Ag and Pd surfaces for the generation of Aubased alloys on both Ag and Pd regions.²⁸ Wang and coworkers leveraged the use of atomically intermixed AuCu₃ and AuCu bimetallic nanoparticles as the sacrificial templates to react with a Au(III) precursor in an aqueous solution.²⁷ They established that the compositional stoichiometry and structural ordering of the Au-Cu nanoparticles played two important roles in controlling the galvanic replacement reaction for the production of complex nanostructures through an interplay of dealloying,^{29–31} Kirkendall diffusion,^{18,32} and Ostwald ripen-

Despite the success in transforming mono- and bimetallic nanocrystals into hollow and/or porous nanostructures through the galvanic replacement reactions, it remains a challenge to spatially confine the oxidation (dissolution) and reduction (deposition) reactions to different sites on the surface of a sacrificial template. Herein, we report a systematic study of the galvanic replacement reactions between various types of precursors and Ag@Ag-Au core-frame nanocubes, a newly developed template with well-defined spatial distributions for Ag and Au on the surface. The replacement reactions were conducted by titrating the precursor into an aqueous suspension of the core-frame nanocubes under ambient conditions and in the presence of cetyltrimethylammonium chloride (CTAC). In an orthogonal manner, the oxidation of Ag was initiated and continued from all of the side faces dominated by Ag atoms, while the resultant metal atoms (e.g., Pt, Pd, or Au) were concurrently deposited along the edges enriched by Au atoms. By controlling the reaction stoichiometry involved, the core-frame nanocubes were transformed into cage cubes with different compositions and hole sizes. For example, with the use of a Pt(IV) precursor such as H₂PtCl₆, Ag oxidation was initiated from the Agdominated regions located at the center of each side face, creating a cavity on each side face of the nanocube. Concomitantly, the Pt atoms derived from the reduction by Ag were deposited on the edges for the generation of a Ag@ Ag-Au-Pt concave nanocube. As the reaction progressed, Ag oxidation was continued in the Ag-dominated region located on each side face rather than those regions where the Ag atoms had formed alloys with Au and/or Pt due to the difference in reduction potentials. Because one Pt atom would be produced at the expense of four Ag atoms during the replacement reaction, it was possible to carve away all Ag atoms from the side faces toward the center in a well-aligned, orthogonal manner. As a result, the Ag@Ag-Au-Pt concave nanocubes

were transformed into nanoscale cage cubes made of a Ag—Au—Pt alloy. The same approach also works for other precursors, including Pt(II), Pd(II), and Au(III), albeit the size and exact location of the hole might vary due to the differences in stoichiometry and reduction potential.

2. EXPERIMENTAL SECTION

- 2.1. Chemicals. Ethylene glycol (EG) was ordered from J.T. Baker. Sodium hydrosulfide hydrate (NaSH-xH2O), aqueous hydrochloric acid (HCl, 37 wt %), poly(vinylpyrrolidone) (PVP) with an average molecular weight of 55000 (PVP-55k), silver trifluoroacetate (CF₃COOAg, ≥99.99% trace-metal basis), gold(III) chloride trihydrate (HAuCl₄·3H₂O, ≥99.9% trace-metal basis), chloroplatinic acid hexahydrate (H₂PtCl₆·6H₂O, ACS reagent, ≥37.50% Pt basis), iron(III) nitrate nonahydrate (Fe(NO₃)₃·9H₂O), potassium tetrachloroplatinate(II) (K₂PtCl₄, ≥99.9% trace-metal basis), sodium tetrachloropalladate(II) (Na₂PdCl₄, ≥99.99% trace-metal basis), aqueous cetyltrimethylammonium chloride solution (CTAC, 25 wt %), and L-ascorbic acid (H2Asc, 99%) were acquired from Sigma-Aldrich (St. Louis, MO). Sodium hydroxide (NaOH, 98%) and acetone (HPLC grade, 99.5+%) were obtained from Alfa Aesar. All chemicals were used as received. All aqueous solutions were prepared using deionized water with a resistivity of 18.2 M Ω ·cm at room temperature.
- **2.2. Synthesis of Ag Nanocubes.** We synthesized Ag nanocubes with an average edge length of 40.5 ± 2.8 nm by following the published protocol.³⁵ After washing the Ag nanocubes with acetone and water, once each, we redispersed them in water for further use.
- 2.3. Synthesis of Ag@Ag-Au Core-Frame Nanocubes. In a standard protocol, the reaction solution was prepared by mixing 2 mL of aqueous CTAC (0.1 M), 0.5 mL of aqueous H₂Asc (0.1 M), and 0.5 mL of aqueous NaOH (0.2 M) under magnetic stirring at 1150 rpm. Next, we added 23 μ L of the aqueous suspension of Ag nanocubes into the reaction solution to attain a final particle concentration of around 2.6 × 10¹¹ particles/mL, followed by the titration of 0.4 or 0.8 mL of aqueous HAuCl₄ (0.1 mM) using a syringe pump at a rate of 0.02 mL/min to two types of core-frame nanocubes, namely, Ag@Ag-Au-4 and Ag@Ag-Au-8. After the titration was completed, we collected nanoparticles at 7200 rpm for 11 min, removed the supernatant, and redispersed them in 100 μ L of water
- **2.4.** Synthesis of the Ag@Ag-Au-Pt Concave Nanocubes and Ag-Au-Pt Cage Cubes. In a standard protocol, we added 100 μ L of the as-prepared Ag@Ag-Au-4 and Ag@Ag-Au-8 nanocubes into a reaction solution containing 2 mL of aqueous CTAC (0.1 M) and 1 mL of water under magnetic stirring at 1150 rpm. Next, we titrated different volumes of aqueous H_2PtCl_6 (0.2 mM) using a syringe pump at a rate of 0.02 mL/min. After the desired volume had been reached, we left the reaction solution under magnetic stirring for about 30 min before the solid products were collected by centrifugation at 7200 rpm for 11 min. We washed the solid products with water twice before they were redispersed in 1 mL of water for further use. The same protocol was also applied to other types of precursors, including K_2PtCl_4 , Na_2PdCl_4 , and $HAuCl_4$ except that different titration volumes were used and $HAuCl_4$ was titrated at the rate of 0.0025 mL/min.
- **2.5. Etching the Ag@Ag-Au Core-Frame Nanocubes with Fe(NO₃)₃.** In a typical process, we added 100 μ L of the as-prepared Ag@Ag-Au-8 nanocubes into a reaction solution containing 2 mL of aqueous CTAC (0.1 M) and 1 mL of water under magnetic stirring at 1150 rpm. Next, we titrated different volumes of aqueous Fe(NO₃)₃ (0.2 or 0.8 mM) using a syringe pump at a rate of 0.02 mL/min. After the desired volume had been reached, we left the reaction solution under magnetic stirring for about 30 min before the solid products were collected by centrifugation at 7200 rpm for 11 min. We then washed the solid products with water twice before they were redispersed in 1 mL of water for further use.
- **2.6.** Instrumentation and Characterization. The particles were collected using an Eppendorf 5430 centrifuge (Eppendorf North

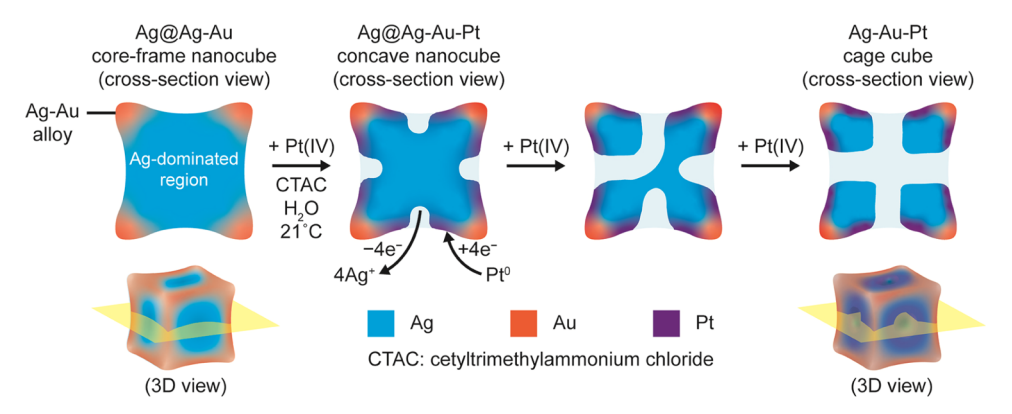


Figure 1. Schematic diagram illustrating the structural evolution of a Ag@Ag-Au core-frame nanocube into a Ag@Ag-Au-Pt concave cube and a Ag-Au-Pt cage cube through a galvanic replacement reaction.

America, Hauppauge, NY). The UV—vis spectra were recorded using a Cary 60 spectrophotometer (Agilent Technologies, Santa Clara, CA). The metal contents were determined using an inductively coupled plasma mass spectrometer (ICP-MS, NexION 300Q, PerkinElmer, Waltham, MA). Transmission electron microscopy (TEM) images were captured on a Hitachi HT7700 microscope (Tokyo, Japan) operated at 120 kV. Scanning electron microscopy (SEM) images were captured on a Hitachi SU8230 field-emission SEM (Tokyo, Japan) operated at 20 kV. High-angle annular dark-field scanning electron microscopy (HAADF-STEM) images were recorded on a Hitachi HD2700 C_s-corrected microscope operated at 200 kV. The energy-dispersive spectroscopy (EDS) detector on the HD2700 was used to generate an elemental mapping of the nanocrystals.

3. RESULTS AND DISCUSSION

We followed our published protocol to synthesize the Ag@ Ag-Au core-frame nanocubes that were composed of a Ag core and a Au-Ag alloy frame. Specifically, we titrated 0.4 and 0.8 mL of aqueous HAuCl4, respectively, into an aqueous suspension of Ag nanocubes in the presence of H2Asc, NaOH, and CTAC to generate Ag@Ag-Au-4 and Ag@Ag-Au-8, respectively. They embraced different amounts of Ag in the core and different thicknesses for the Ag-Au frame, in addition to different degrees of concaveness on their side faces. We then used the core-frame nanocubes as sacrificial templates to react with a salt precursor such as H_2PtCl_6 in the presence of CTAC. Finally, we analyzed the products using electron microscopy and UV-vis spectroscopy to examine both the structural and compositional changes during the course of the galvanic reaction.

Figure 1 shows a plausible pathway for the gradual transformation of a Ag@Ag-Au core-frame nanocube into a Ag@Ag-Au-Pt concave nanocube and then a Ag-Au-Pt cage cube through a galvanic replacement reaction. In the first step, Ag oxidation would preferentially start from the Agdominated regions located in the center of each side face to create a cavity, while the resultant Pt atoms are deposited on the edges and corners of the nanocube, leading to the generation of a Ag@Ag-Au-Pt concave nanocube. As the galvanic reaction is continued, holes are continuously drilled in all side faces in an orthogonal but well-aligned manner, while Pt atoms are concurrently deposited on the edges and corners, followed by interdiffusion and alloying with Ag and Au atoms. Once a thin layer of Ag-Au-Pt alloy is formed on the surface, including the areas around but not inside the cavities, Ag oxidation can be confined to the center of each side face, making it possible to continuously remove all Ag in the core

for the generation of a Ag-Au-Pt cage cube. There are some differences between the cases of Ag@Ag-Au-4 and Ag@Ag-Au-8 core-frame nanocubes. For example, in the latter case, the concaveness of the side faces is increased so that it becomes much easier to drill through the core even in the early stage of synthesis. On the other hand, the greater coverage of Au on the side faces of the core-frame nanocube will significantly reduce the area of the Ag-dominated region for better confinement of Ag oxidation to the center of each side face, leading to the generation of cage cubes containing smaller through-holes.

In the first set of experiments, we examined the structural and compositional evolutions of Ag@Ag-Au-4 nanocubes after they had reacted with different volumes of H₂PtCl₆ in the presence of CTAC by transmission electron microscopy (TEM). Figure 2A shows a TEM image of the initial coreframe nanocubes, indicating slight concaveness on their side

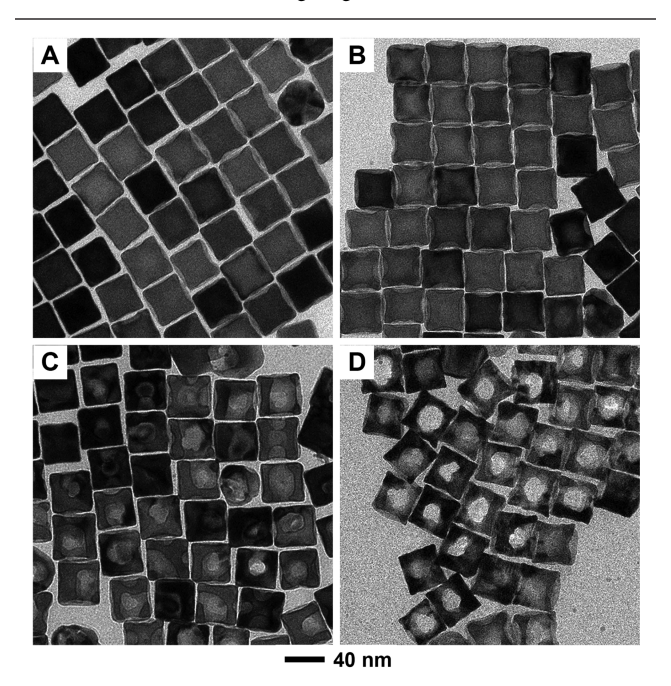


Figure 2. TEM images of (A) the Ag@Ag-Au-4 core-frame nanocubes prepared by reacting 0.4 mL of 0.1 mM aqueous $HAuCl_4$ with Ag nanocubes and (B-D) the solid products obtained by further titrating different volumes of aqueous H_2PtCl_6 (0.2 mM) into the suspension in the presence of CTAC. The titration volumes were (B) 0.1, (C) 0.4, and (D) 1.2 mL, respectively.

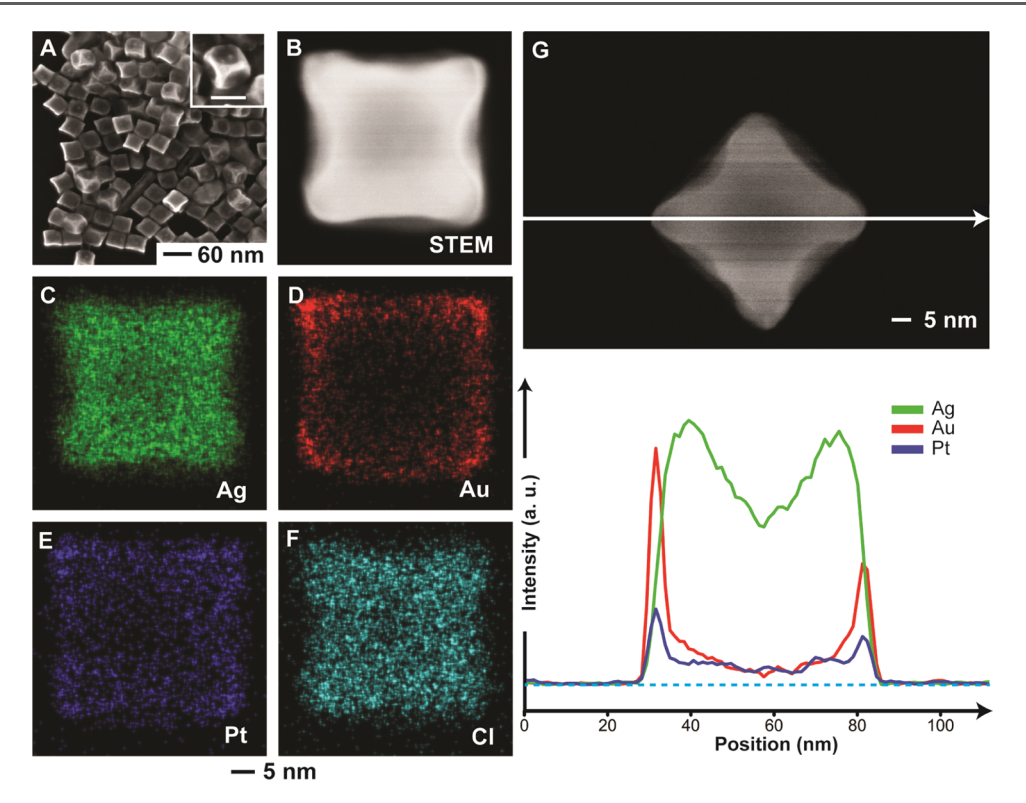


Figure 3. (A) SEM image of the Ag@Ag—Au—Pt concave nanocubes as shown in Figure 2B (the inset scale bar is 40 nm) and (B) HAADF-STEM image of a single concave nanocube. (C—F) EDS mapping of the particle in (B), showing the signals from (C) Ag, (D) Au, (E) Pt, and (F) Cl, respectively. (G) HAADF-STEM image of the particle in (B) but with the raster angle rotated by 45° and the corresponding EDS line-scan profiles of Ag, Au, and Pt, respectively.

faces. At 0.1 mL of H₂PtCl₆, Figure 2B shows their transformation into more concaved nanostructures, primarily due to the preferential oxidation of Ag atoms by Pt(IV) precursor from the center of each side face. At 0.4 mL of H₂PtCl₆, Figure 2C shows a mixture of nanocubes with different numbers of holes drilled in their side faces. This result suggests that the oxidation rates of different side faces likely differed from each other due to the variations in terms of the surface defect and coverage density of a capping agent such as Cl⁻ ions derived from CTAC. When the titration volume was increased to 1.2 mL, Figure 2D indicates that the product consisted of cage cubes with orthogonal, well-aligned throughholes, confirming that Ag oxidation was more or less confined to the center of each side face.

To gain a better understanding of the onset of Ag oxidation on the side faces of Ag@Ag-Au core-frame nanocubes, we used scanning electron microscopy (SEM) and aberrationcorrected high-angle annular dark-field scanning TEM (HAADF-STEM) to characterize the sample prepared with the addition of 0.1 mL of H₂PtCl₆ (i.e., the same shown in Figure 2B). Figure 3A shows the SEM image of the sample, in which the cavities on the side faces could be easily identified. Figure 3B shows a HAADF-STEM image collected from one nanocube that was orientated along the (001) zone axis, confirming the presence of concaveness on the side faces. We also performed energy-dispersive X-ray spectroscopy (EDS) mapping on the same particle to resolve the spatial distributions of Ag, Au, Pt, and Cl elements. As shown in Figure 3C-F, Ag followed the contour of the particle, while both Au and Pt were largely confined to the edges and corners only. The signal of Pt was rather weak when compared with those of Ag and Au due to the limited amount of the deposited

Pt. The Cl signal followed the trend of the Ag signal, suggesting that the CTAC-derived Cl⁻ ions could selectively bind to the Ag{100} facets, consistent with other findings.^{22,23}

We also characterized the same particle by EDS linescanning analysis to better understand the spatial distributions of Ag, Au, and Pt elements. As shown in Figure 3G, the line profile of Ag shows a dip in the center of the particle, confirming the concaveness on the side face. On the other hand, the line profiles of Au and Pt indicate that both Au and Pt atoms were concentrated on the edges and corners of the particle, leaving the side faces still dominated by Ag. Because Au cannot react with Pt(IV), we argue that the Au signal should reflect the original Au distribution on the surface of the Ag@Ag-Au-4 nanocube, consistent with our previous findings.²⁴ Altogether, we believe that the galvanic replacement reaction was initiated through the oxidation of Ag from the Agdominated regions located at the center of each side face due to the selective binding of Cl⁻ ions to Ag{100} facets for the deposition of Pt on the edges and corners in an orthogonal manner for the generation of Ag@Ag-Au-Pt concave nanocubes. Based on the inductively coupled plasma mass spectrometry (ICP-MS) analysis, these trimetallic concave nanocubes had an elemental composition of Ag₈₆Au₁₂Pt₂.

In the second set of experiments, we replaced the Ag@Ag—Au-4 nanocubes with Ag@Ag—Au-8 nanocubes to increase the thickness of the frames while keeping all other experimental conditions unchanged. Figure 4A shows the SEM of the Ag@ Ag—Au-8 nanocubes, confirming more concaved side faces when compared with those of Ag@Ag—Au-4 nanocubes (see Figure 2A). With the addition of 0.1 mL of H₂PtCl₆, Figure 4B indicates the formation of small holes localized at the center of each side face, which was completely different from the

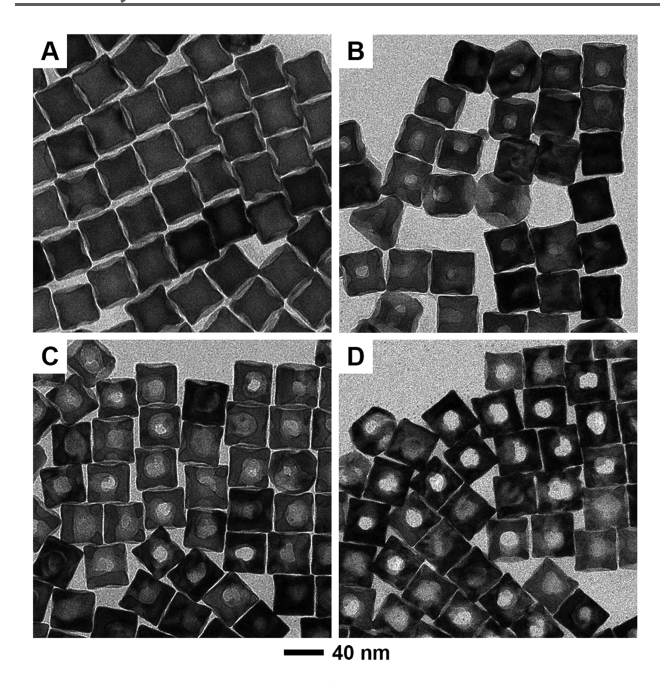


Figure 4. TEM images of (A) the Ag@Ag-Au-8 core-frame nanocubes prepared by reacting 0.8 mL of aqueous HAuCl₄ (0.1 mM) with Ag nanocubes, and (B-D) the products obtained by titrating different volumes of aqueous $\rm H_2PtCl_6$ (0.2 mM) into the asobtained suspension of Ag@Ag-Au-8 nanocubes in the presence of CTAC. The titration volumes were (B) 0.1, (C) 0.4, and (D) 1.2 mL, respectively.

product obtained by reacting the Ag@Ag-Au-4 nanocubes with the same amount of H_2PtCl_6 (Figure 2B). As the reaction progressed to 0.4 mL of H_2PtCl_6 , Figure 4C shows the formation of holes on most of the side faces in a nonuniform manner, consistent with our previous observation (see Figure 2C). At 1.2 mL, Figure 4D indicates the formation of cage cubes containing orthogonal, well-aligned through-holes.

We further investigated the detailed structure and composition of the nanoframes shown in Figure 4D. Figure 5A,B shows the SEM image of the sample and the HAADF-STEM image of one nanoframe that was orientated along the (001) zone axis, respectively, confirming the highly open structure. Figure 5C-F shows the spatial distributions of Ag, Au, Pt, and Cl, respectively, in the nanoframe. Again, the Ag signal overlapped with the profile of the particle, while the Au signal was predominantly distributed at the edges and corners of the particle. On the other hand, both the Pt and Cl signals were distributed across the entire surface of the particle. Figure 5G shows the corresponding EDS line profiles of Ag, Au, and Pt, respectively. It was found that the Au signal was mostly distributed on the edges and corners with an extension toward the center of the particle, supporting our argument that more Au was deposited on the side faces of the Ag@Ag-Au-8 nanocubes than that of the Ag@Ag-Au-4 nanocubes. On the other hand, the Ag signal was rather weak due to the significant loss of Ag at this point of the reaction. The Pt line profile overlapped with the Au line profile, suggesting the deposition of Pt on the Au-enriched regions on the particle during the galvanic reaction. There was a thin layer of Pt around the holes, together with Au and Ag, making the alloy regions less reactive toward Ag oxidation from these areas. As marked by

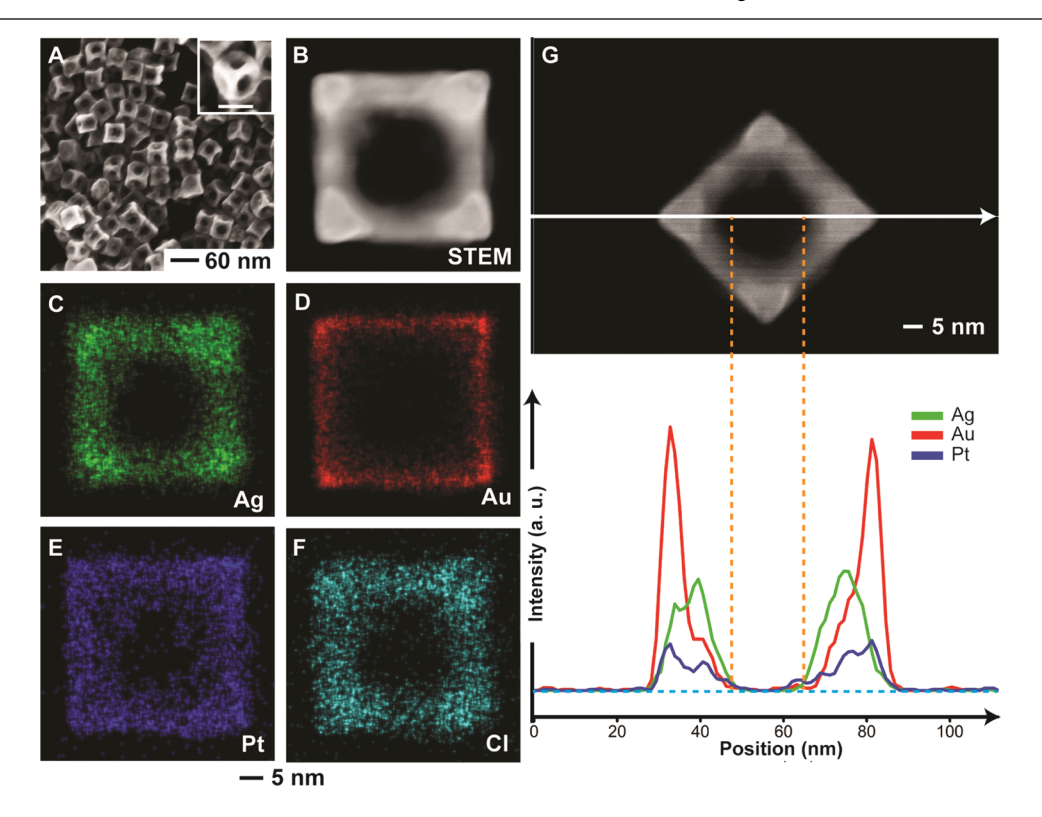


Figure 5. (A) SEM image of the Ag—Au—Pt cage cubes as shown in Figure 3D (the inset scale bar is 40 nm) and (B) HAADF-STEM image of a single cage cube. (C—F) EDS mapping of the particle in (A), showing the signals from (C) Ag, (D) Au, (E) Pt, and (F) Cl, respectively. (G) HAADF-STEM image of the same particle in (A) but with the raster angle rotated by 45° and the corresponding EDS line-scan profiles of Ag, Au, and Pt, respectively.

two orange dotted lines, there were essentially very little signals for Ag, Au, and Pt inside the hole, indicating that the Ag drilling process indeed penetrated through the entire thickness of the particle. The diameter of the hole was estimated to be around 25 nm. The ICP-MS data gave a composition of Ag₇₃Au₂₃Pt₄ for the trimetallic cage cubes.

Our TEM results demonstrate that both Ag@Ag-Au-4 and Ag@Ag-Au-8 nanocubes could be transformed into cage cubes made of Ag-Au-Pt alloy through a galvanic replacement reaction. We further used UV-vis spectroscopy to follow the reaction in an attempt to reveal the subtle differences arising from the difference in Au distribution on the surface of the Ag@Ag-Au nanocubes because the localized surface plasmon resonance (LSPR) properties of Ag-Au alloy nanocrystals are extremely sensitive to the change from solid to hollow nanostructures. ^{36,37} Figure 6A shows the UV-vis

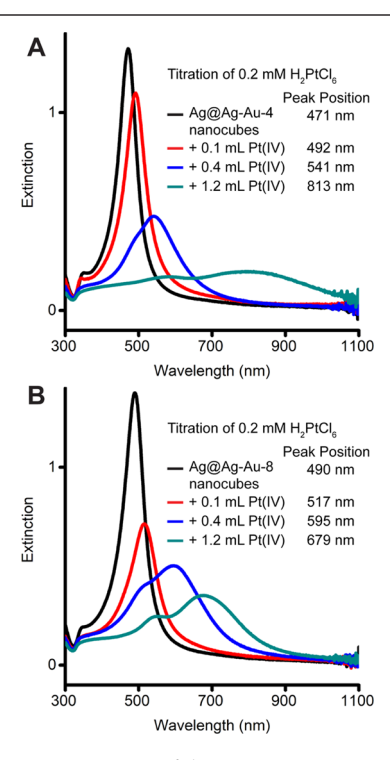


Figure 6. (A) UV–vis spectra of the Ag@Ag–Au-4 nanocubes before and after reacting with different volumes of aqueous H_2PtCl_6 (0.2 mM). (B) UV–vis spectra of the Ag@Ag–Au-8 nanocubes before and after reacting with different volumes of aqueous H_2PtCl_6 (0.2 mM).

spectra of the Ag@Ag-Au-4 nanocubes before and after reacting with 0.1, 0.4, and 1.2 mL of H₂PtCl₆. It was found that the major LSPR peak of the Ag@Ag-Au-4 nanocubes was located at 471 nm, together with a narrow bandwidth. After reacting with 0.1 mL of H₂PtCl₆, the peak was red-shifted to 492 nm, with a slight decrease in peak intensity and a little broadening in peak width, attributing to the concave morphology of nanocrystals. At 0.4 mL, the LSPR peak was further red-shifted to 541 nm, together with a drastic decrease in peak intensity and a significant broadening in peak width, due to the emergence of cavities on the side faces of the nanocubes. At 1.2 mL, the LSPR peak became extremely weak and broad, with the peak position shifted to 813 nm, corresponding to the formation of Ag-Au-Pt cage cubes.

In comparison, Figure 6B shows the UV-vis spectra of Ag@ Ag-Au-8 nanocubes before and after reacting with 0.1, 0.4, and 1.2 mL of H₂PtCl₆. The nanocubes exhibited a major peak at 490 nm because of more concaveness on the side faces. At 0.1 mL of H₂PtCl₆, the LSPR peak was red-shifted to 517 nm, together with an increase in peak width and a decrease in peak intensity. These LSPR characteristics would be attributed to the formation of cavities, consistent with the TEM results (Figure 4B). As the volume of H₂PtCl₆ was increased to 0.4 and 1.2 mL, we noticed that the peak was continuously redshifted to 595 and 679 nm, respectively, together with a shoulder peak at 500 nm. These results indicate that the two final products would consist of two populations, consistent with the TEM images (see Figure 4C,D). It is worth mentioning that, after reacting the Ag@Ag-Au-8 nanocubes with 1.2 mL H₂PtCl₆, the major peak position was located at 679 nm, while the peak was positioned at 813 nm after reacting the Ag@Ag-Au-4 nanocubes with the same amount of H₂PtCl₆. Although there is little difference in the TEM images shown in Figures 2D and 4D, our UV-vis data suggest that the holes were better confined to the center of the cubes derived from the Ag@Ag-Au-8 nanocubes than those derived from Ag@Ag-Au-4. Taken together, we believe that the amount of Ag located in the core of the Ag@Ag-Au core-frame nanocubes, together with the distribution of Au on the surface of a cubic template, could direct the galvanic replacement reaction to produce either Ag@Ag-Au-Pt concave nanocubes or Ag-Au-Pt cage cubes, respectively.

We also argue that the drilling of Ag could become efficient by complementing Ag oxidative etching at the center of each side face of a nanocube with the deposition of Pt atoms onto the edges and corners in an orthogonal manner. To support our hypothesis, we performed another set of experiments by replacing H₂PtCl₆ with Fe(NO₃)₃ in the standard protocol while leaving other parameters unchanged. We chose Fe-(NO₃)₃ because the galvanic replacement reaction between Ag@Ag-Au-8 nanocubes and Fe(NO₃)₃ would produce one Fe(II) ion at the expense of one Ag and leaving this ion in the reaction solution but not depositing on the template. Figure 7A shows the UV-vis spectra of the Ag@Ag-Au-8 nanocubes before and after reacting with 0.2, 0.4, 1.2, and 2.8 mL of 0.2 mM Fe(NO₃)₃. We noticed that the major LSPR peak of the Ag@Ag-Au-8 nanocubes was only shifted from 490 nm to 503 nm at the end of the titration process, which is completely different from the results obtained from the use of 0.2 mM H₂PtCl₆ (Figure 5B). Figure 7B shows the TEM image of the final product with some cavities on the surface of the concave nanocubes, indicating that the etching of Ag was rather slow. To increase the etching rate, we increased the concentration of Fe(NO₃)₃ from 0.2 to 0.8 mM. Under this condition, Figure 7C shows that the major LSPR peak of the Ag@Ag-Au-8 nanocubes was shifted from 490 to 494, 513, 534, and 540 nm at the titration volumes of 0.4, 1.2, 2.8, and 4.0 mL, respectively. Although Figure 7D shows the formation of small holes localized at the center of nanocubes in the sample prepared by 4.0 mL of Fe(NO₃)₃ (0.8 mM), this morphology is still very different from the cage cube nanostructures produced from the reaction of Ag@Au-Ag-8 nanocubes with 1.2 mL of H₂PtCl₆ (0.2 mM) (Figure 3C). Altogether, we conclude that it would be difficult to use $Fe(NO_3)_3$ to remove Ag uniformly from the Ag-dominated regions of Ag@Ag-Au nanocubes for the generation of cage cube nanostructures through the galvanic replacement reaction. Part of the

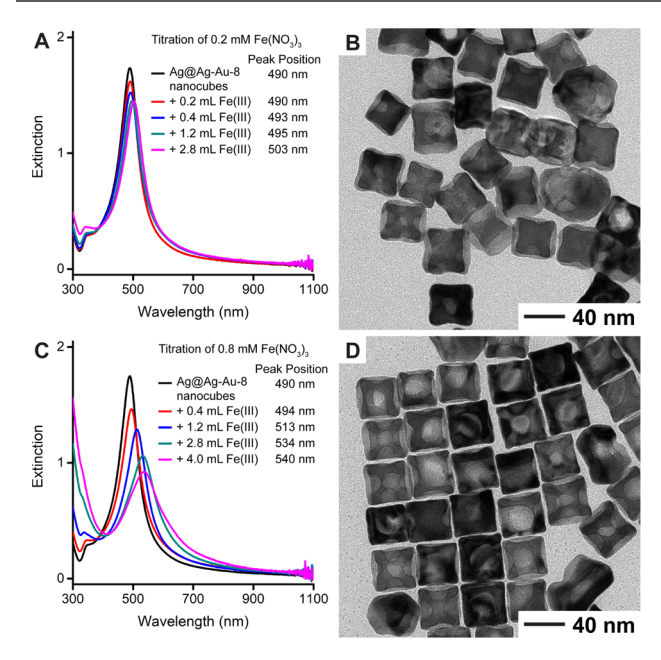


Figure 7. (A) UV–vis spectra of the Ag@Ag–Au-8 nanocubes before and after reacting with different volumes of aqueous Fe(NO₃) $_3$ (0.2 mM). (B) TEM image of the sample prepared by reacting 2.8 mL of aqueous Fe(NO₃) $_3$ (0.2 mM) with Ag@Ag–Au-8 nanocubes. (C) UV–vis spectra of the Ag@Ag–Au-8 nanocubes before and after reacting with different volumes of aqueous Fe(NO₃) $_3$ (0.8 mM). (D) TEM image of the sample prepared by reacting 4.0 mL of aqueous Fe(NO₃) $_3$ (0.8 mM) with the Ag@Ag–Au-8 nanocubes.

challenges arises from the delocalized carving of Ag across the entire surface of Ag@Ag—Au nanocubes during the reaction, suggesting that the deposition of a third metal such as Pt on the template could help confine the oxidative etching of Ag at the center more effectively.

We further extended the same strategy to the production of cage cubes with holes in different sizes by reacting the Ag@ Ag-Au-8 nanocubes with other types of salt precursors, including K2PtCl4, Na2PdCl4, and HAuCl4. In these experiments, we followed the standard protocol except for the replacement of H₂PtCl₆ with another precursor. It is worth acknowledging that the reaction between the Ag@Ag-Au-8 nanocubes and H2PtCl6 was rather slow. For example, with the titration of 1.2 mL of H₂PtCl₆ (0.2 mM), our ICP-MS analysis indicated that 71% of the Pt(IV) would remain in the reaction solution at the time point of 30 min. Figure S1A gives the UV-vis spectra of the sample before and after the reaction had progressed for 240 min. It was found that the LSPR peak of the Ag@Ag-Au nanocubes was further red-shifted to 736 nm when compared with the peak located at 679 nm (Figure 6B). Figure S1B shows a TEM image of the product, implying the transformation of the Ag@Ag-Au nanocubes into nanocages. In comparison, the reaction between the Ag@Ag-Au-8 nanocubes with other precursors would complete within 30 min because the UV-vis spectra showed almost no change beyond this time point. Under this circumstance, we titrated smaller volumes of the new precursors into the reaction solution.

Figure 8A shows the UV–vis spectra of Ag@Ag–Au-8 nanocubes before and after reacting with 0.2 mL K_2 PtCl₄ (0.2 mM), from which we observed the red shift of the major LSPR peak from 490 to 515 nm. Figure 8B gives a TEM image of the product that includes some cage cubes with relatively small

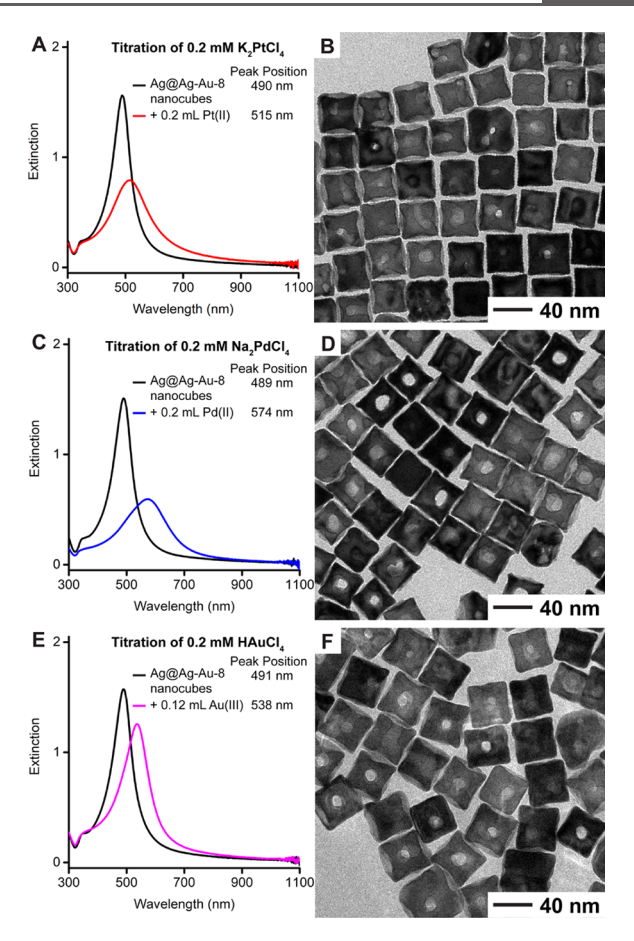


Figure 8. (A) UV-vis spectra of the Ag@Ag-Au-8 nanocubes before and after reacting with 0.2 mL of aqueous K₂PtCl₄ (0.2 mM). (B) TEM image of the product. (C) UV-vis spectra of the Ag@Ag-Au-8 nanocubes before and after reacting with 0.2 mL of aqueous Na₂PdCl₄ (0.2 mM). (D) TEM image of the product. (E) UV-vis spectra of the Ag@Ag-Au-8 nanocubes before and after reacting with 0.12 mL of aqueous HAuCl₄ (0.2 mM). (F) TEM image of the product.

holes in the center. Because one Pt atom was generated at the expense of two Ag atoms during the galvanic replacement between Ag and Pt(II) precursors, we argue that the carving of Ag would become less efficient, leading to the formation of smaller holes. When the titration volume was increased from 0.2 to 0.4 mL, we noticed that the major LSPR peak was shifted from 490 to 511 nm (Figure S2A), similar to the trend shown in Figure 8A. As shown by the TEM image in Figure S2B, Ag was also removed from regions other than the center for the formation of pits on the side faces of a nanocube. Different from H₂PtCl₆, K₂PtCl₄ could react with Ag in the Ag—Pt alloy region through the galvanic replacement reaction, making it more difficult to confine the drilling of Ag to the center of each side face.

When we replaced the Pt(II) with a Pd(II) precursor such as Na_2PdCl_4 , Figure 8C shows the UV-vis spectra of the Ag@ Ag-Au-8 nanocubes before and after reacting with 0.2 mL of Na_2PdCl_4 (0.2 mM), indicating more significant red shift of the major LSPR peak from 489 to 574 nm. Figure 8D shows a TEM image of the product, revealing the generation of cage cubes with holes larger than those derived from K_2PtCl_4 . Such a change could be attributed to the difference in reduction potential between these two precursors. As the titration volume was increased to 0.4 mL, the LSPR peak was further

shifted to 628 nm (Figure S3A). The TEM image in Figure S3B indicates the formation of nanoframes with rough edges. We also conducted an experiment with HAuCl₄ for the generation of bimetallic cage cubes. Because Au(III) is very easy to be reduced and the galvanic replacement reaction would produce one Au at the expense of three Ag atoms, we used a smaller titration volume and a slower titration rate. Figure 8E shows the UV-vis spectra of the Ag@Ag-Au-8 nanocubes before and after reacting with 0.12 mL of HAuCl₄ (0.2 mM). It was found that the LSPR peak was changed from 491 to 538 nm. Based on the TEM image in Figure 8F, cage cubes were also obtained. As the titration volume was increased to 0.24 mL, the LSPR peak was further shifted to 586 nm (Figure S4A). The TEM image in Figure S4B indicates the formation of pits on the side faces of a nanocube. Similar to the case of Pt(II), Au also interdiffuses with Ag for the formation of a Ag-Au alloy. Taken together, our results suggest that it is possible to tailor the experimental conditions such as the concentration of the precursor and the titration rate to optimize the galvanic replacement reaction or the generation of cage cubes. The size of the holes would strongly depend on the stoichiometry involved, as well as the reduction potential of the precursor.

4. CONCLUSIONS

In summary, we developed a facile route to the generation of multimetallic cage cubes by drilling through all of the side faces of Ag nanocubes. Our success relies on the use of Ag@Ag-Au core-frame nanocubes with Ag in the core and Ag-Au alloy frames along the corners and edges of a nanocube to confine the drilling of Ag to the center of each side face and ultimately to align the intersected holes with the center of the nanocube. In a typical protocol, we dispersed Ag@Ag-Au core-frame nanocubes in an aqueous solution containing CTAC, followed by the titration of an aqueous solution of a salt precursor such as H₂PtCl₆, K₂PtCl₄, Na₂PdCl₄, or HAuCl₄ under ambient conditions. Depending on the stoichiometry and reduction potential of the salt precursor, a simple galvanic replacement reaction between the Ag@Ag-Au nanocubes and the precursor could produce multimetallic cage cubes with holes of different sizes. At the early stage of a synthesis, because the Cl⁻ ions derived from CTAC could bind the selectivity toward the Ag(100) surface, the oxidation of Ag would preferentially be started from the Ag-dominated regions located at the center of each side face of a nanocube for the creation of a cavity, while the resultant metal atoms are deposited on the edges and corners in an orthogonal manner. As the Ag atoms are removed from the side faces in the form of Ag(I) ions for the generation of other metals followed by their deposition on the edges and corners of nanocubes, we could achieve the continuous carving of Ag atoms from the center of a coreframe nanocube for its ultimate transformation into a cage cube enclosed by a Ag-Au-Pt, Ag-Au-Pd, or Ag-Au alloy, together with three orthogonal, intersected holes. We believe that these multimetallic cage cubes will find their potential applications in plasmonics and catalysis. They also could serve as templates to assemble smaller spheres such as polystyrene beads for the fabrication of hybrid nanostructures.

ASSOCIATED CONTENT

S Supporting Information

The Supporting Information is available free of charge on the ACS Publications website at DOI: 10.1021/acs.chemmater.9b03774.

UV—vis spectra of Ag@Ag—Au-8 nanocubes before and after reacting with 0.2 mM H₂PtCl₆ for 240 min and the TEM image of resultant nanostructures; UV—vis spectra of Ag@Ag—Au-8 nanocubes before and after reacting with 0.2 mM K₂PtCl₄, Na₂PdCl₄, or HAuCl₄, and the corresponding TEM images of the final products, respectively (PDF)

AUTHOR INFORMATION

Corresponding Author

*E-mail: dong.qin@mse.gatech.edu.

ORCID ®

Dong Qin: 0000-0001-5206-5912

Notes

The authors declare no competing financial interest.

ACKNOWLEDGMENTS

The authors acknowledge the support from the National Science Foundation (CHE-1708300) and start-up funds from the Georgia Institute of Technology (GT). The authors thank for helpful discussions with Dr. Peng Wang and Daniel Wang. The characterization work was performed, in part, at the Georgia Tech Institute for Electronics and Nanotechnology, a member of the National Nanotechnology Coordinated Infrastructure (NNCI), which is supported by the National Science Foundation (Grant ECCS-1542174).

■ REFERENCES

- (1) Rosi, N. L.; Mirkin, C. A. Nanostructures in Biodiagnostics. *Chem. Rev.* **2005**, *105*, 1547–1562.
- (2) Huang, X.; El-Sayed, I. H.; Qian, W.; El-Sayed, M. A. Cancer Cell Imaging and Photothermal Therapy in the Near-Infrared Region by Using Gold Nanorods. *J. Am. Chem. Soc.* **2006**, *128*, 2115–2120.
- (3) Xia, Y.; Li, W.; Cobley, C. M.; Chen, J.; Xia, X.; Zhang, Q.; Yang, M.; Cho, E. C.; Brown, P. K. Gold Nanocages: From Synthesis to Theranostic Applications. *Acc. Chem. Res.* **2011**, *44*, 914–924.
- (4) Kim, S.-W.; Kim, M.; Lee, W. Y.; Hyeon, T. Fabrication of Hollow Palladium Spheres and Their Successful Application to the Recyclable Heterogeneous Catalyst for Suzuki Coupling Reactions. *J. Am. Chem. Soc.* **2002**, *124*, 7642–7643.
- (5) Zeng, J.; Zhang, Q.; Chen, J.; Xia, Y. A Comparison Study of the Catalytic Properties of Au-Based Nanocages, Nanoboxes, and Nanoparticles. *Nano Lett.* **2010**, *10*, 30–35.
- (6) Mahmoud, M. A.; Narayanan, R.; El-Sayed, M. A. Enhancing Colloidal Metallic Nanocatalysis: Sharp Edges and Corners for Solid Nanoparticles and Cage Effect for Hollow Ones. *Acc. Chem. Res.* **2013**, *46*, 1795–1805.
- (7) Mahmoud, M. A.; El-Sayed, M. A. Gold Nanoframes: Very High Surface Plasmon Fields and Excellent Near-Infrared Sensors. *J. Am. Chem. Soc.* **2010**, *132*, 12704–12710.
- (8) Pérez-Juste, J.; Pastoriza-Santos, I.; Liz-Marzán, L. M.; Mulvaney, P. Gold nanorods: Synthesis, characterization and applications. *Coord. Chem. Rev.* **2005**, 249, 1870–1901.
- (9) Xie, H.-N.; Larmour, I. A.; Smith, W. E.; Faulds, K.; Graham, D. Surface-Enhanced Raman Scattering Investigation of Hollow Gold Nanospheres. *J. Phys. Chem. C* **2012**, *116*, 8338–8342.
- (10) Yang, Y.; Zhang, Q.; Fu, Z.-W.; Qin, D. Transformation of Ag Nanocubes into Ag-Au Hollow Nanostructures with Enriched Ag

Contents to Improve SERS Activity and Chemical Stability. ACS Appl. Mater. Interfaces 2014, 6, 3750–3757.

- (11) Schlücker, S. Surface-Enhanced Raman Spectroscopy: Concepts and Chemical Applications. *Angew. Chem., Int. Ed.* **2014**, 53, 4756–4795.
- (12) Liu, K.; Bai, Y.; Zhang, L.; Yang, Z.; Fan, Q.; Zheng, H.; Yin, Y.; Gao, C. Porous Au–Ag Nanospheres with High-Density and Highly Accessible Hotspots for SERS Analysis. *Nano Lett.* **2016**, *16*, 3675–3681
- (13) Chen, J.; McLellan, J. M.; Siekkinen, A.; Xiong, Y.; Li, Z.-Y.; Xia, Y. Facile Synthesis of Gold-Silver Nanocages with Controllable Pores on the Surface. *J. Am. Chem. Soc.* **2006**, *128*, 14776–14777.
- (14) Sun, Y.; Mayers, B.; Xia, Y. Metal Nanostructures with Hollow Interiors. *Adv. Mater.* **2003**, *15*, 641–646.
- (15) Zhang, W.; Yang, J.; Lu, X. Tailoring Galvanic Replacement Reaction for the Preparation of Pt/Ag Bimetallic Hollow Nanostructures with Controlled Number of Voids. *ACS Nano* **2012**, *6*, 7397–7405.
- (16) Sutter, E.; Jungjohann, K.; Bliznakov, S.; Courty, A.; Maisonhaute, E.; Tenney, S.; Sutter, P. In situ liquid-cell electron microscopy of silver—palladium galvanic replacement reactions on silver nanoparticles. *Nat. Commun.* **2014**, *5*, No. 4946.
- (17) Hong, J. W.; Kang, S. W.; Choi, B.-S.; Kim, D.; Lee, S. B.; Han, S. W. Controlled Synthesis of Pd—Pt Alloy Hollow Nanostructures with Enhanced Catalytic Activities for Oxygen Reduction. *ACS Nano* **2012**, *6*, 2410—2419.
- (18) González, E.; Arbiol, J.; Puntes, V. F. Carving at the Nanoscale: Sequential Galvanic Exchange and Kirkendall Growth at Room Temperature. *Science* **2011**, 334, 1377–1380.
- (19) Ruditskiy, A.; Xia, Y. The Science and Art of Carving Metal Nanocrystals. ACS Nano 2017, 11, 23–27.
- (20) Zhang, H.; Jin, M.; Wang, J.; Li, W.; Camargo, P. H. C.; Kim, M. J.; Yang, D.; Xie, Z.; Xia, Y. Synthesis of Pd-Pt Bimetallic Nanocrystals with a Concave Structure through a Bromide-Induced Galvanic Replacement Reaction. J. Am. Chem. Soc. 2011, 133, 6078–6089
- (21) Goris, B.; Polavarapu, L.; Bals, S.; Van Tendeloo, G.; Liz-Marzán, L. M. Monitoring Galvanic Replacement Through Three-Dimensional Morphological and Chemical Mapping. *Nano Lett.* **2014**, *14*, 3220–3226.
- (22) Zhang, J.; Liu, J.; Xie, Z.-X.; Qin, D. HAuCl4: A Dual Agent for Studying the Chloride-Assisted Vertical Growth of Citrate-Free Ag Nanoplates with Au Serving as a Marker. *Langmuir* **2014**, *30*, 15520–15530.
- (23) Zhou, S.; Li, J.; Gilroy, K. D.; Tao, J.; Zhu, C.; Yang, X.; Sun, X.; Xia, Y. Facile Synthesis of Silver Nanocubes with Sharp Corners and Edges in an Aqueous Solution. *ACS Nano* **2016**, *10*, 9861–9870.
- (24) Ahn, J.; Wang, D.; Ding, Y.; Zhang, J.; Qin, D. Site-Selective Carving and Co-Deposition: Transformation of Ag Nanocubes into Concave Nanocrystals Encased by Au–Ag Alloy Frames. *ACS Nano* **2018**, *12*, 298–307.
- (25) Luo, Z.; Ahn, J.; Qin, D. Fabrication of Ag–Pd concave nanocrystals through facet-selective oxidation of Ag atoms. *Nanoscale* **2019**, *11*, 6710–6718.
- (26) Chen, A. N.; McClain, S. M.; House, S. D.; Yang, J. C.; Skrabalak, S. E. Mechanistic Study of Galvanic Replacement of Chemically Heterogeneous Templates. *Chem. Mater.* **2019**, *31*, 1344–1351.
- (27) Li, G. G.; Sun, M.; Villarreal, E.; Pandey, S.; Phillpot, S. R.; Wang, H. Galvanic Replacement-Driven Transformations of Atomically Intermixed Bimetallic Colloidal Nanocrystals: Effects of Compositional Stoichiometry and Structural Ordering. *Langmuir* **2018**, 34, 4340–4350.
- (28) Lutz, P. S.; Bae, I.-T.; Maye, M. M. Heterostructured Au/Pd—M (M = Au, Pd, Pt) nanoparticles with compartmentalized composition, morphology, and electrocatalytic activity. *Nanoscale* **2015**, *7*, 15748–15756.

- (29) Williams, D. E.; Newman, R. C.; Song, Q.; Kelly, R. G. Passivity breakdown and pitting corrosion of binary alloys. *Nature* **1991**, *350*, 216–219.
- (30) Erlebacher, J.; Aziz, M. J.; Karma, A.; Dimitrov, N.; Sieradzki, K. Evolution of nanoporosity in dealloying. *Nature* **2001**, *410*, 450–453.
- (31) Li, X.; Chen, Q.; McCue, I.; Snyder, J.; Crozier, P.; Erlebacher, J.; Sieradzki, K. Dealloying of Noble-Metal Alloy Nanoparticles. *Nano Lett.* **2014**, *14*, 2569–2577.
- (32) Nakajima, H. The discovery and acceptance of the Kirkendall Effect: The result of a short research career. *IOM* **1997**, 49, 15–19.
- (33) Viswanatha, R.; Sarma, D. D. In *Nanomaterials Chemistry: Recent Developments and New Directions*, Rao, C. N. R.; Müller, A.; Cheetham, A. K., Eds.; Wiley-VCH: Weinheim, Germany, 2007; Chapter 4, pp 139–170.
- (34) Zhang, Z.; Wang, Z.; He, S.; Wang, C.; Jin, M.; Yin, Y. Redox reaction induced Ostwald ripening for size- and shape-focusing of palladium nanocrystals. *Chem. Sci.* **2015**, *6*, 5197–5203.
- (35) Skrabalak, S. E.; Au, L.; Li, X.; Xia, Y. Facile synthesis of Ag nanocubes and Au nanocages. *Nat. Protoc.* **2007**, *2*, 2182–2190.
- (36) Kelly, K. L.; Coronado, E.; Zhao, L. L.; Schatz, G. C. The Optical Properties of Metal Nanoparticles: The Influence of Size, Shape, and Dielectric Environment. *J. Phys. Chem. B* **2003**, *107*, 668–677
- (37) Tao, A. R.; Habas, S.; Yang, P. Shape Control of Colloidal Metal Nanocrystals. *Small* **2008**, *4*, 310–325.